Sensors & Actuators: B. Chemical 346 (2021) 130555

Contents lists available at ScienceDirect

Sensors and Actuators: B. Chemical

journal homepage: www.elsevier.com/locate/snb

Carbon dots as multifunctional platform for intracellular pH sensing and bioimaging. *In vitro* and *in vivo* studies

Jorge Espina-Casado [a,1], Tania Fontanil [b,c,d,1], Alfonso Fernández-González [a], Santiago Cal [b,d], Álvaro J. Obaya [d,e], Marta Elena Díaz-García [a], Rosana Badía-Laíño [a,*]

[a] Departamento de Química Física y Analítica, Universidad de Oviedo, Oviedo, Asturias, 33006, Spain
[b] Departamento de Bioquímica y Biología Molecular, Universidad de Oviedo, 33006, Oviedo, Spain
[c] Departamento de Investigación, Instituto Ordóñez, Oviedo, Asturias, 33012, Spain
[d] Instituto Universitario de Oncología, IUOPA, Universidad de Oviedo, 33006, Oviedo, Spain
[e] Departamento de Biología Funcional, Área de Fisiología, Universidad de Oviedo, 33006, Oviedo, Spain

ARTICLE INFO

Keywords:
Carbon dots
Chemosensor
Intracellular pH
Bioimaging
Theranostic

ABSTRACT

In the present work we have obtained carbon dots (CDs) from glutathione and modified their surface with both β-Cyclodextrin and methyl-3-(4-(2-(5-((methylsulfonyl)oxy)pentyl)- 1,3-dioxo -2,3-dihydro- 1H-benzo[de]isoquinolin -6-yl)piperazin-1-yl)propanoate (FP), a pH-sensitive molecule. β-Cyclodextrin acted as a glucose source, which facilitated the entrance of the CDs within the cells and, eventually, can be used as drug-carrier to deploy bioactive compounds in the cytoplasm. FP fluorescence varied according to the pH of the medium and can be used to distinguish cancer cells due to the Warburg effect.

Cytotoxicity studies revealed that, contrarily to simple CDs, carbon nanodots modified with β-cyclodextrins had an impact in cell cycle phase distribution, with no alterations of cell morphology. Likewise, CDs modified with β-cyclodextrin and FP can be used to distinguish cancer cells from non-cancerous ones due to an increase in fluorescent emission. Furthermore, this modified CDs can also be used to obtain high contrast *in vitro* images as well as *in vivo* images. These results demonstrate the potential applications of the synthetized nanoparticles both in bioimaging and as theranostic sensor and actuator.

1. Introduction

Research on carbon-based nanoparticles, particularly carbon-dots (CDs), has received a strong boost due to the particular properties of these materials, such as their interesting luminescent characteristics (high quantum yields, photostability, tunable emission wavelength), their high solubility and stability in water, biodegradability and their very low or even null cytotoxicity [1]. In addition to the possibility of their obtaining through easy, low-cost and "green" methods, these materials show the advantage of possessing surface functional groups which can be further modified for particular applications [2,3]. The surface functionalization and/or passivation process during synthesis is one of the main methods used to control the fluorescent properties of CDs, thanks to the modification of the surface emissive sites [4]. Due to their unique photoluminescence properties, carbon dots offer a potential alternative to the traditional fluorescent dyes in applications such as intra-cell probes, in-vivo labelling and/or bioimaging [5,6]. In fact, over the past ten years scientists have made great strides towards the use of raw native CDs as (bio)sensing materials while the use of hybrid CDs composites are still scarce. So, for example, it has been reported that the fluorescent dye Rhodamine B can be attached to the surface of CDs to develop a ratiometric probes to detect Fe^{3+} in lake and tap waters [7] or histidine [8]. Wang et al. [9] dispersed CDs modified with Rhodamine B into agarose gels to develop a hydrogel sensing film for semiquantitative visual detection of Hg(II) under a UV lamp. Recently, Yu et al. [10] described the "off-on-off" detection of CN-, hydroquinone and ascorbic acid using CDs modified with coumarin.

On the other hand, the CDs modification with cyclodextrins (CyDs) for their use in (bio)analytical applications using "turn-off", "turn-on", "turn-off-on" and host-guest recognition approaches for selected bioanalytes has also been described [11–14].

In the present work we have designed a novel system based on

* Corresponding author.
E-mail address: rbadia@uniovi.es (R. Badía-Laíño).
[1] These authors contributed equally to this work.

https://doi.org/10.1016/j.snb.2021.130555
Received 26 May 2021; Received in revised form 21 July 2021; Accepted 2 August 2021
Available online 4 August 2021

glutathione-based carbon dots (CD) capped with both pH (fluorescent 1,8-naphthylamide-based dye, **FP**) and drug delivery (β-cyclodextrin, βCyD) functions (**FP**-**CD**-βCyD). As cancer cell excrete lactic acid, cancerous environments have acidic pH values [15]. The fluorescent **FP** dye exhibits pH-dependent fluorescence emission [16] and we leveraged this function for the *in-vitro* determination of intracellular pH in the melanoma-derived murine cell line B16F10 in comparison with noncancerous human mammary fibroblasts (HMF). In addition, *in vivo* analysis of body CDs distribution was also performed and analyzed by *in vivo* fluorescence imaging. Our results indicate that, the β-cyclodextrin moiety can act as a potential carrier for drug delivery; and that CDs, may act as a *bone fide* tool as bioimaging reporters. Therefore, the main objective of this work is to characterize **FP**-**CD**-βCyDs for optical pH sensing and imaging application for *in vitro* and *in vivo* bioanalyses.

2. Experimental

2.1. Reagents and instrumentations

2.1.1. Reagents and materials

N-(3-Dimethylaminopropyl)-N′-ethylcarbodiimide hydrochloride (EDC·HCl), sodium N-hydroxysulfosuccinimide (sulfo-NHS), 4-aminophenylboronic acid (APBA), Tris(hydroxymethyl)aminomethane (TRIS), β-cyclodextrin (βCyD), ethylenediaminetetraacetic acid (EDTA), formaldehyde, 2-[4-(2-hydroxyethyl)-1-piperazinyl-(1)]ethanesulfonic (HEPES), propidium iodide, Triton X-100, NaCl, KCl, $CaCl_2$, $MgSO_4$, NaH_2PO_4, ethanol, pyridine and sodium acetate were purchased form Sigma. Phosphate buffer solution 1X pH 7.4 (PBS), trypsin and glucose were purchased from Merck. Milli-Q water (MQW) was used throughout the experimental. 3.5 kDa Membrane Dialysis Tubes were from Merck.

Dulbecco's Modified Eagle Medium (DMEM), fetal bovine serum (FBS), penicillin, streptomycin, glutamine, Sorting buffer (PBS, 5 mM EDTA, 25 mM HEPES, pH 7.0), and ribonuclease A were purchased from Gibco. Xylazine (Rompun) was purchased from Bayer and Ketamine (Imalgene) from Boehringer Ingelheim. Kit Cell Titer 96 Non-Radioactive Cell Proliferation Assay was from Promega. 35 μm filter labbox, Silicone culture-insert 2 well and μ-Dish 35 were supplied by Ibidi®.

2.1.2. Spectrophotometric instrumentation

FTIR spectra were recorded in a Varian 670 spectrometer, using 4 cm^{-1} at 2000 cm^{-1} resolution and 32 scans per sample. The photoluminescence spectra of molecular compounds and nanomaterials were recorded with an Edinburgh Instruments FLSP-920 spectrofluorimeter. Fluorescence quantum yield was measured on Edinburgh Instruments FS-5 with an integrating sphere using solutions in such concentrations that their absorbance at the excitation wavelength was kept below 0.1. Absorbance measurements were carried out in a Biotek PowerWave XS multiplayer VIS / UV absorption spectrophotometer using 96-well plates.

Fluorescence intensity of nanomaterials in cultured cells was measured using a Biotek Hybrid Synergy H4 multiplate fluorimeter by exciting at 350 nm and emission at 430 nm. *In vivo* fluorescence bioimages were acquired on a Xenogen IVIS Imaging System (MA, USA) at 520 nm (GFP filter) using 430 nm as excitation wavelength, exposure of 1 min and pixel binning set at 4. Images from tissue samples were obtained in a Leica TCS-SP8X confocal fluorescence microscope (Heidelberg, Germany) using a 405 nm laser diode and the emitted fluorescence detected with a photomultiplier tube detector.

Detection of fluorescent nanoparticles within living cells was analysed on a Beckman Coulter Cytoflex S cytometer and their effect on cell cycle phase distribution was carried out on a Beckman Coulter Cytomics FC500 cytometer (CA, USA). Images from cultured cells were obtained in a Zeiss Axiovert 200 m inverted microscope using 3 excitation wavelengths 365, 436 and 546 nm.

2.2. Synthesis of the new nanomaterial

Raw carbon dots (CDs) were synthesized as described by Díaz-Faes et al. [17]. Functionalization of CDs with β-cyclodextrin was carried out as reported by S. Mondal et al. [18] with some modifications.

a Functionalization of CDs with 4-aminophenylboronic acid, **CD**-APBA

10 mL of Milli-Q water were added to a Schlenk flask containing 0.4 g of CDs and the mixture was sonicated in an ultrasound bath for 18 min. Then, the flask was connected to a stream of N_2 and sonication continued for 2 more min. 38.4 mg (0.2 mmol) of N-(3-dimethylaminopropyl)-N′-ethylcarbodiimide hydrochloride (EDC·HCl) and 43.4 mg (0.2 mmol) of sodium N-hydroxysulfosuccinimide (sulfo-NHS) were added and allowed to react 1 h with constant stirring at 360 rpm, at room temperature under a N_2 atmosphere. Finally, 31.6 mg (0.2 mmol) of 4-aminophenylboronic acid were introduced into the foregoing reaction. The mixture was continuously stirred at room temperature for 48 h. Lastly, the solvent was evaporated on a rotatory evaporator under reduced pressure. The visible orange solid was purified by dispersion in 5 mL of ethanol, centrifugation at 5000 r.p.m for 10 min and removal of the supernatant. The process was repeated 3 times to obtain the **CD**-APBA. 0.13 g of **CD**-APBA were obtained.

b Functionalization of **CD**-APBA with β cyclodextrin, **CD**-βCyD

0.13 g of **CD**-APBA were dispersed in 5 mL of 0.1 M tris(hydroxymethyl)aminomethane (TRIS) buffer at pH 10.4. Then, 1 mL of a saturated solution of βCyD in 0.1 M TRIS buffer pH 10.4 was added and the mixture was continuously stirred at 360 rpm for 12 h. Thereafter, the solvent was removed using a rotatory evaporator under reduced pressure. The obtained solid was dispersed in 5 mL of ethanol in an ultrasonic bath, centrifuged at 5000 rpm and the supernatant discarded. This sequence was repeated three times and 0.08 g of **CD**-βCyD, a light brown solid, was finally obtained.

c Functionalization of **CD**-βCyD with methyl-3-(4-(2-(5-((methylsulfonyl)oxy)pentyl)-1,3-dioxo-2,3-dihydro-1H-benzo[de]isoquinolin-6-yl)piperazin-1-yl)propanoate, **FP**-**CD**-βCyD

The surface functionalization of CD in the ensemble CD-βCyD with a pH-sensitive fluorescent probe (**FP**, methyl-3-(4-(2-(5-((methylsulfonyl)oxy)pentyl)-1,3-dioxo-2,3-dihydro-1H-benzo[de]isoquinolin-6-yl)piperazin-1-yl)propanoate was carried out following the steps described by Espina et al. [16] (See supplementary Information), obtaining 0.03 g of a dark orange solid, **FP**-**CD**-βCyD.

2.3. In vitro studies

Three cell lines were used to analyze CDs-cell interaction: the murine melanoma cell line B16F10, the human osteosarcoma cell line U2OS and human mammary fibroblasts HMF. B16F10 and U2OS were kindly provided by Dr Carlos López-Otín (Universidad de Oviedo) and the HMF cell line was purchased from Innoprot. All cells were routinely cultured in an incubator at 37 °C, in a 5 % CO_2 atmosphere and in DMEM medium containing 10 % heat-inactivated fetal bovine serum, supplemented with 100 U/mL penicillin and 50 μg/mL streptomycin from Gibco Life Technologies (Complete Cell Medium). These incubation conditions and cell medium composition are described as Standard Conditions throughout the text.

2.3.1. Cell culture and MTT assay

To quantify the effect of CDs on cell proliferation, B16F10 and U2OS were employed. To this end, the kit Cell Proliferation Assay (Promega) was used following manufacturer's instructions. In brief, 5000 cells/well were seeded in 96-well plates and exposed to free CDs and **CD**-βCyDs at

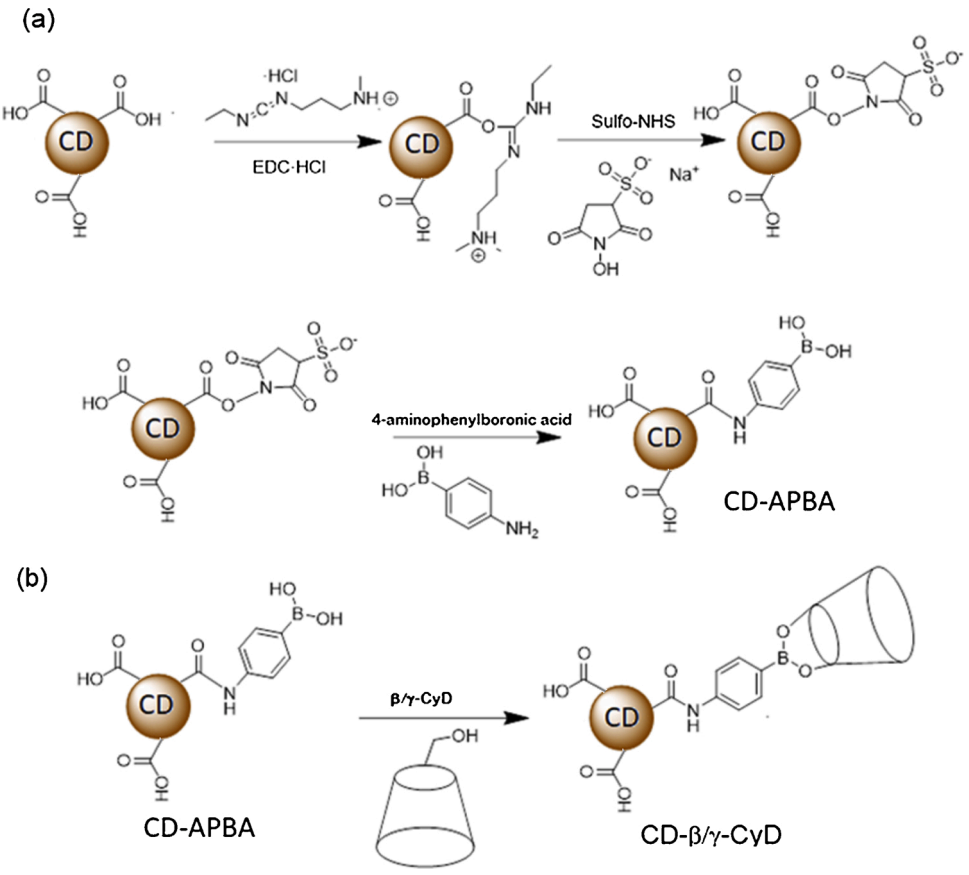

Fig. 1. Surface modification of CDs with βCyDs.

concentrations of 0.0, 0.01, 0.1, 0.5, 1.0 and 2.0. mg mL^{-1} resuspended in Complete Cell Medium from a 10 mg mL^{-1} stock solution in PBS during 5 days at 37 °C and 5 % CO_2. Cell proliferation was measured by the conversion of 3-(4,5-dimethylthiazol-2-yl)-5-(3-carboxymethoxyphenyl)-2-(4-sulfophenyl)-2H-tetrazolium (MTT) into formazan water soluble compound. Absorbance can be then measured at 570 nm using a Synergy H4 Hybrid reader. Each condition was performed in sextuplets.

2.3.2. *Fluorescence imaging*

5×10^5 B16F10 and HMF cells were cultured on cover glasses within 24-well plates (Menzel-Gläser, Germany) and allowed to attach for 24 h (Standard Conditions). Cells were then incubated in the presence of 1 mg mL^{-1} solution of free CDs or **CD**-βCyDs in Complete Cell Medium for 60 min under the same conditions. Then, media was removed, and cells washed 3 times with PBS pH 7.4. Finally, cells were fixed with 4% formaldehyde and mounted with Vectashield Antifade Mounting Medium.

2.3.3. *Flow cytometry*

B16F10, U2OS and HMF cells were cultured in 6-well plates in the presence of 1 $mg.mL^{-1}$ of CDs for 1 h in Complete Cell Medium. After the incubation, cells were washed three times with PBS and detached from the well with a solution containing 0.25 % trypsin, 0.5 mM EDTA in DMEM. Following centrifugation (433×*g*), cells were re-suspended at a concentration of 1×10^6 cells/mL in 500 μL of Sorting Buffer enriched with 2 % fetal bovine serum. Samples were filtered through a 35 μm filter before each cytometer measurement to remove cell aggregates.

For cell cycle phase distribution studies, after 1 h incubation with CDs in the above conditions, tripsynised U2OS and HMF cells were washed three times with PBS, fixed with 80 % ethanol and kept at 4 °C until analysis was performed. For cytometric analysis, cells were centrifuged to remove ethanol and re-suspended in 250 μL PBS. Finally, 2 mg of ribonuclease A and 0.2 mL of 1 mg mL^{-1} propidium iodide were added. Cell cycle distribution was analysed in a Beckman Coulter Cytomics FC500 cytometer.

2.3.4. *Intracellular pH by bioimaging*

U2OS cells were cultured in the presence of 2×10^{-5} M **FP-CD-**βCyDs during 15 min in Standard Conditions. Then, cells were washed three times with PBS and fixed with 4 % v/v formaldehyde. Finally, images were taken in a Leica SP8 confocal microscope using a 405 nm laser and after 30 min incubation with high potassium cation regulators (30 mM NaCl, 120 mM KCl, 1 mM $CaCl_2$, 0.5 mM $MgSO_4$, 1 mM NaH_2PO_4, 5 mM glucose, 20 mM HEPES, 20 mM sodium acetate) at pH 6.0 and at pH 7.4.

2.4. *In vivo studies*

To perform *in vivo* studies, six 24-week-old C57BI/6J mice were used, housed under SPF (Specific Pathogen Free) conditions and according to the guidelines of the Animal Experimentation Committee of the University of Oviedo. They were distributed into two groups (n = 3), with one of them used as a control. All experiments and procedures with animals were carried out following the European Directive 2012/63/EU and following the indications of the Animal Experimentation facility of Universidad de Oviedo.

2.4.1. *Fluorescence bioimaging*

Mice anesthetized with ketamine (50 mg kg^{-1} body weight) and xylazine (10 mg kg^{-1} body weight) were used for *in vivo* fluorescence bioimaging. Once anesthetized, a dose of 2 mg kg^{-1} animal of **FP-CD-**βCyD in PBS was injected through the lateral tail veins. Fluorescent distribution throughout the body was observed with the Xenogen IVIS Imaging System over a period of 1 h. To analyse specific organs, one hour after the intravenous injection of the nanomaterials, mice were

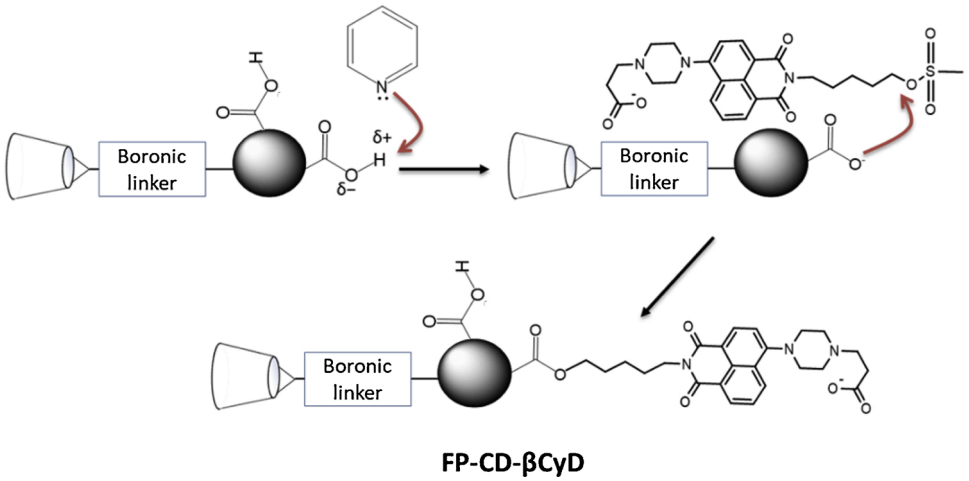

Fig. 2. Reaction pathway to obtain the ditopic assembly **FP**-**CD**-βCyD.

sacrificed in a CO_2 chamber. Liver, lung, kidney and heart were removed and immediately fixed in a 4 % formaldehyde saline solution for 24 h. Organs were then washed with 70 % ethanol and embedded in paraffin blocks. Before measuring fluorescence, samples were deparaffinized and treated with 0.1 % Triton X-100 to permeabilize and 0.1 M glycine to decrease autofluorescence.

3. Results and discussion

3.1. Synthesis and functionalization of carbon dots

Raw CDs obtained by a hydrothermal synthesis from glutathione and citric acid [17] have been selected in this work due to their interesting characteristics, mainly, a) high luminescence quantum yield with no photobleaching drawbacks [19], an interesting characteristics for bio-imaging applications; b) low cytotoxicity [20], c) antioxidant activity [21], and d) an easily modifiable surface due to the presence of the glutathione and citric acid functional groups (—COOH, NH—$_2$ and S—H). Due to the presence of these surface groups, it was possible to sequentially modify glutathione-citric acid based CDs with different functions. So, in a first step, the covalent bond of βCyD was achieved by activation of surface C—OOH groups using a carbodiimide (EDC·HCl) reaction forming an amine-reactive O-acyl isourea intermediate which was then stabilized by the addition of sulfo-NHS, forming a sulfo-NHS ester more stable and efficient for conjugation to primary amines, APBA in the present case. As a result, the CDs were grafted with a thin organic layer of APBA (**CD**-APBA) (Fig. 1a), which further reacted with hydroxyl groups of the βCyD forming stable cyclic boronate esters [22], to render the **CD**-βCyD (Fig. 1b).

The ATR-FTIR spectrum of **CD**-βCyD (Fig. S1) shows the characteristic bands from their precursor compounds, which suggest an efficient functionalization. Thus, sharp band between 3300–3500 cm^{-1}, assignable to stretching vibrations of O—H bonds, can be clearly observed in CyD as well in the **CD**-βCyD spectra, while in raw CDs the band is unsharpened broad and weak. On the other hand, characteristic bands of βCyD can be observed in **CD**-βCyD such as the band at 2917 cm^{-1}, assigned to stretching vibrations of groups with C in sp^3 hybridization (—CH and C—H_2) and the band at 1152 cm^{-1} the vibration of the COC—— (cyclic ether) group. The peak appearing at 1700 cm^{-1} in CD and CD-βCyD spectra can be attributed to carboxylic groups on CD surface (from glutathione/citrate), although in the CD-βCyD the intensity of this band decreased significantly indicating a possible involvement of the APBA linker. The peak appearing at 1577 cm^{-1} was assigned to the flexion of the NH group and stretching of the CN—— group (amide, glutathione). Peaks at 1384 cm^{-1} and 996 cm^{-1} were assigned due to the asymmetric stretching of the B—O group and the deformation of the BOH group, respectively. These data, therefore, proved the participation of all precursors used in the synthesis of CD-——βCyD. The comparative FTIR band assignment of precursors and final functionalized CDs are shown in Table S1. On the other side, HRTEM images demonstrated that the functionalization did not affect significantly the spherical morphology nor affected the original size of the raw CDs, being the nanoparticle diameter in the 3 ± 2 nm range both for CD and CD-βCyD (Fig. S2). In a second step, we performed a further functionalization of **CD**-βCyD with the fluorescent probe **FP**. This reaction was carried out in pyridine as solvent. Pyridine also acted as reaction activator, that is, the basic pyridine-like nitrogen ability to accept protons from the —COOH groups on the CD surface which, in turn favored the carboxylates nucleophilic attack of carboxylates to the carbon bound to the mesylate group of the dye. As a final result, the bi-functional ensemble **FP**-**CD**-βCyD was obtained (Fig. 2).

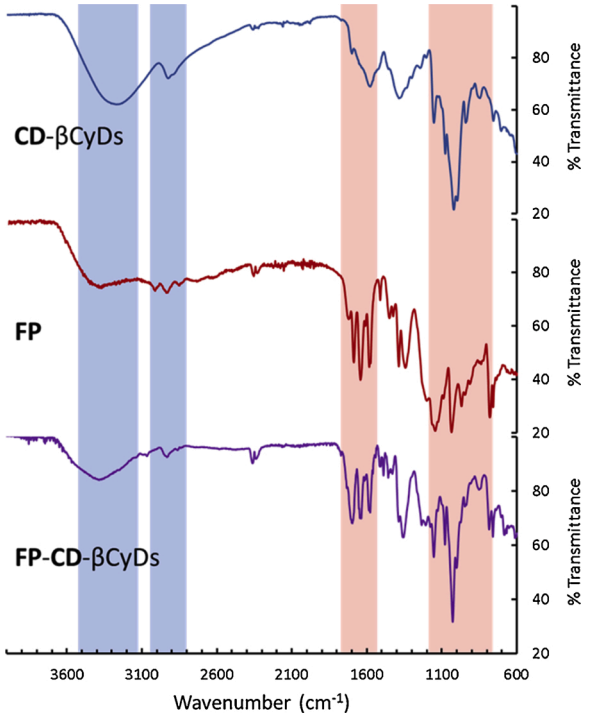

Fig. 3. ATR-FTIR spectra for **FD**-**CD**-βCyD and its main precursors.

ATR-FTIR spectra of the bi-functional assembly exhibited characteristic peaks of the fluorescent probe FP (Fig. 3). The peaks at 1684 and

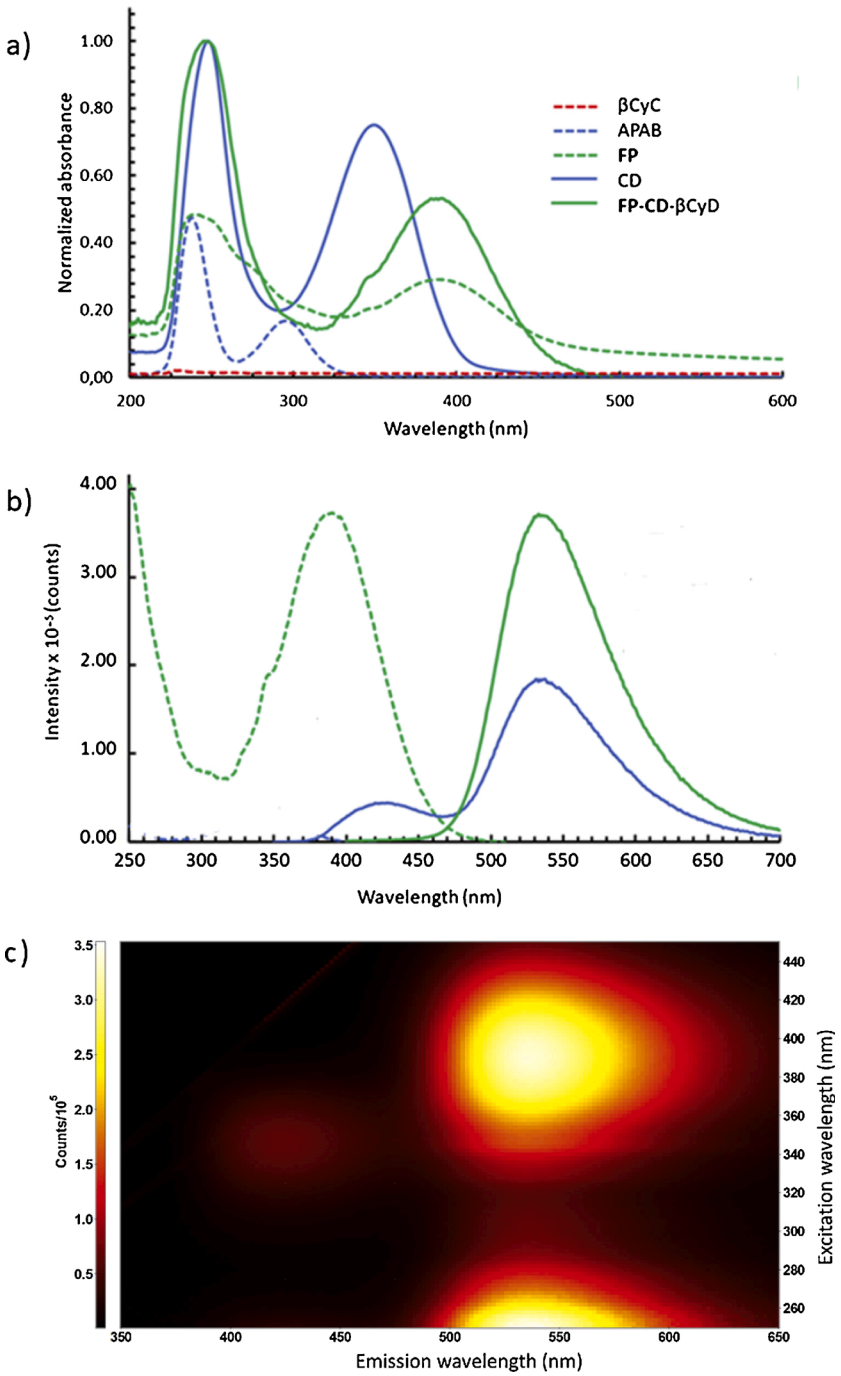

Fig. 4. a) Normalized absorption UV-Vis spectra of **FP-CD**-βCyD and their precursors: beta-cyclodextrin (βCyD), 4-aminophenylboronic acid (APAB), fluorescent probe (**FP**) and CDs. b) Excitation and photoemission spectra of **FP-CD**-βCyD: λ_{exc} 395 nm (green line) and λ_{exc} 345 nm (blue line). c) Contour plot of an excitation-emission matrix for the **FP-CD**- β-CyD ensemble.

1645 cm^{-1} due to CO═ stretching of amide groups, peaks at 1350 or 1151 cm^{-1} ascribed to ester acyl groups and peaks at 750–780 cm^{-1} assigned to aromatic rings. Besides, it is worth to note that in **FP-CD**-βCyD the peaks at 1199 cm^{-1} and 1145 cm^{-1} (S═O symmetric stretching) and that at 1089 cm^{-1} (from S—O flexion) characteristics of the methanesulfonate leaving group are absent, thus suggesting an efficient functionalization (Fig. 3, Table S1).

3.2. Spectroscopic characterization

Fig. 4a shows the absorption spectra of CDs and **FP-CD**-βCyD together with those of the chemicals used for functionalization. Raw CDs spectrum exhibits a dominating absorption band at 248 nm assigned to π-π* transitions in sp2 dominions of CC and NC═══ bonds in CD [23] and a less intense band at 356 nm ascribed to π-π* transitions of surface plasmon states corresponding to CO═ bonds [24,25]. The **FP-CD**-βCyD shows an intense band centered at 248 nm somewhat broader than that of the raw CDs, due to the overlapping bands from APAB at 237 nm (π-π* transitions of CC═ phenyl bond) and at 294 nm from the CN n-σ* transitions. This suggests that APAB was successfully attached to the CD surface and supports the FTIR data. As can be seen in the Fig. 4a, the absorption band of FP could also contribute to the broadening due to its band at 240 nm. **FP-CD**-βCyD also presented an absorption band at 393 nm, characteristic of the FP, which supported that the dye has been

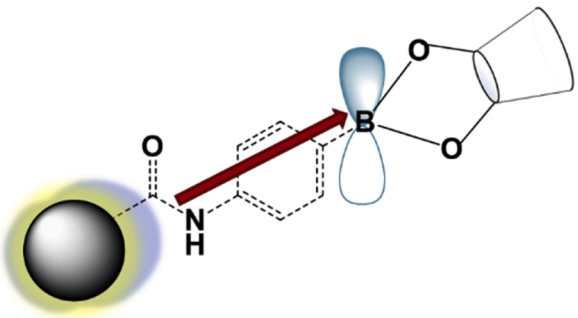

Fig. 5. Boron electron-withdrawing effects on the CDs surface states.

Table 1
Absolute quantum yields bands of the different synthetized nanomaterials.

Nanomaterial	λ_{ex}, nm	λ_{em}, nm	Absolute quantum yield, %
CDs	350	440	49
CD-βCyD	356	430	35
FP-CD	350	445	51
	395	535	16
FP-CD-βCyD	345−350	425	21
	395	533	60

successfully attached to the CDs.

The fluorescence excitation spectra of **FP-CD**-βCyD (Fig. 4b) showed an intense excitation band with a maximum intensity at 395 nm and a weak shoulder at 345 nm consistent with the relevant Vis-UV absorption bands. The fluorescent emission spectra of **FP-CD**-βCyD in Fig. 4b show that excitation at 395 nm (long wavelength absorption band of FP) shows a single emission band centred at 535 nm, whereas excitation at 345 nm leads to a very weak emission band centred at 446 nm, due to the excitation in-between the absorption bands of **CD**-βCyD (see Fig. S3) and a more intense band from **FP** centred at 536 nm. In accordance with this, the simultaneous presence of two luminescent centres in **FP-CD**-βCyD does not seem to influence the position of the main emission band. This can be also seen in the 2D excitation-emission contour map for the FP-CD-βCyD ensemble (Fig. 4c).

Upon excitation at 356 nm, the quantum yield of **CD**-βCyD resulted to be 35 %, lower than that from neat CDs, (49 % when excited at 350 nm) that could be ascribed to the presence of the boronic group close to the CD surface. As βCyDs were not directly bound to the CDs surface but to peripheral boronic groups, their influence on the CDs luminescent properties should be marginal. However, the proximity to the CDs surface of boron atoms, archetypal Lewis acids due to an empty *p* orbital, makes them act as electron-withdrawing inductive groups over neighbouring donating groups on the CDs surface, such $–NH_2$, -OH and –SH. The surface electronic states of the CDs may change as result of those inductive and resonance effects (Fig. 5) which, in turn, can affect the electronic band structure of the CDs lowering significantly (approximately 30 %) the quantum yield of **CD**-βCyD in comparison to neat CDs.

On the other hand, the photoluminescence quantum yield of the bifunctional ensemble **FP-CD**-βCyD resulted to be 21 % when excited at 345−350 nm and increased to 60 % when excited at 395 nm. According to these data (Table 1), we conclude that when **FP-CD**-βCyD were excited in the range 345−350 nm (excitation maxima of neat CDs) the influence of the boron effect manifested itself as a low quantum yield. However, the high quantum yield upon excitation at 395 nm (excitation maximum of FP) could be ascribed to the presence of βCyD moieties that provided a protective restricted environment to the FP molecules from collisional quenching. In fact, in absence of βCyD, the quantum yield of the the **FP-CD** system decreased to 16 % upon excitation at 395 nm (Table 1).

3.3. *pH response and in vitro studies*

In aqueous solution, the **FP-CD**-βCyD ensemble showed a similar response to pH to that of FP-CD, thus suggesting that the presence of the cyclodextrin moiety did not modify its ability to recognize H^+ ions through a PET process [16]. The profile of the **FP-CD**-βCyD fluorescence intensity *versus* pH (excitation at 395 nm) showed a linear response in the interval pH 2–9 with a correlation coefficient 0.998 and a high sensitivity, around 100 fluorescence units/pH unit (Fig. S4). To determine the fitness of **FP-CD**-βCyD as fluorescent intracellular pH probe or as a bio-imaging dye, any potentially harmful cytotoxic effect must be evaluated. For that purpose, cytotoxicity was checked using B16F10 cells incubated in the presence of CDs, **CD**-βCyDs or **FP-CD**-βCyDs at 1 mg mL^{-1} for 1 h. A cell culture without nanoparticles was employed as control. The optical microscope images (Fig. 6) did not show significant differences in cell morphology, which suggest that CDs do not alter cell integrity under the assayed conditions.

Cell proliferation studies [26], evaluated through the mitochondrial activity of cells using the MTT assay, were carried out by exposing B16F10 and U2OS cell lines to different concentrations of nanoparticles from 0.01 to 2.0 mg mL^{-1} for 96 h. Presence of **CD**-βCyDs and **FP-CD**-βCyDs induced low toxicity at lower concentrations (0.01−0.1 mg mL^{-1}) towards B16F10 cells which was comparable to that of free CDs. At higher concentrations and larger exposure times, **CD**-βCyDs and **FP-CD**-βCyDs induced higher toxicity than that of free CDs (Fig. 7). Similar response profiles were observed for U2OS cells (Fig. S5), even though U2OS were more sensitive to both, **CD**-βCyDs and **FP-CD**-βCyDs, than B16F10 cells. In fact, B16F10 showed a cell viability of 90 % with concentrations as high as 0.1 mg mL^{-1}, whereas U2OS show this cell viability till the range of 0.01 mg mL^{-1}. On the other hand, while free CDs caused no apparent damage on any of the two cell lines within the concentration range studied, no differences in cell-induced toxicity between **CD**-βCyDs and **FP-CD**-βCyDs were observed. These results seem to suggest that the presence of the βCyD moiety on the **FP-CD**-βCyD surface is responsible for the observed toxic effect, rather than the fluorescent

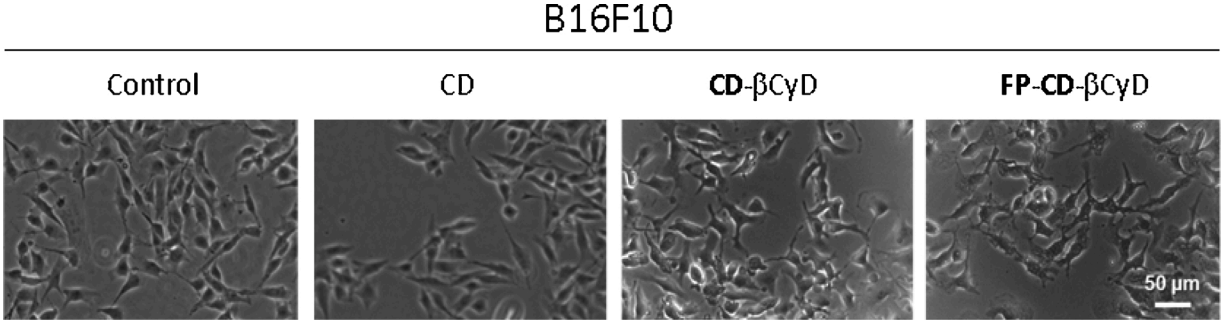

Fig. 6. Phase contrast microscopy images of control B16F10 cells in the absence (control) and in the presence of 1 mg/mL of CDs, **CD**-βCyD and **FP-CD**-βCyD for 1 h at 37 °C. Images were taken with a 20× objective.

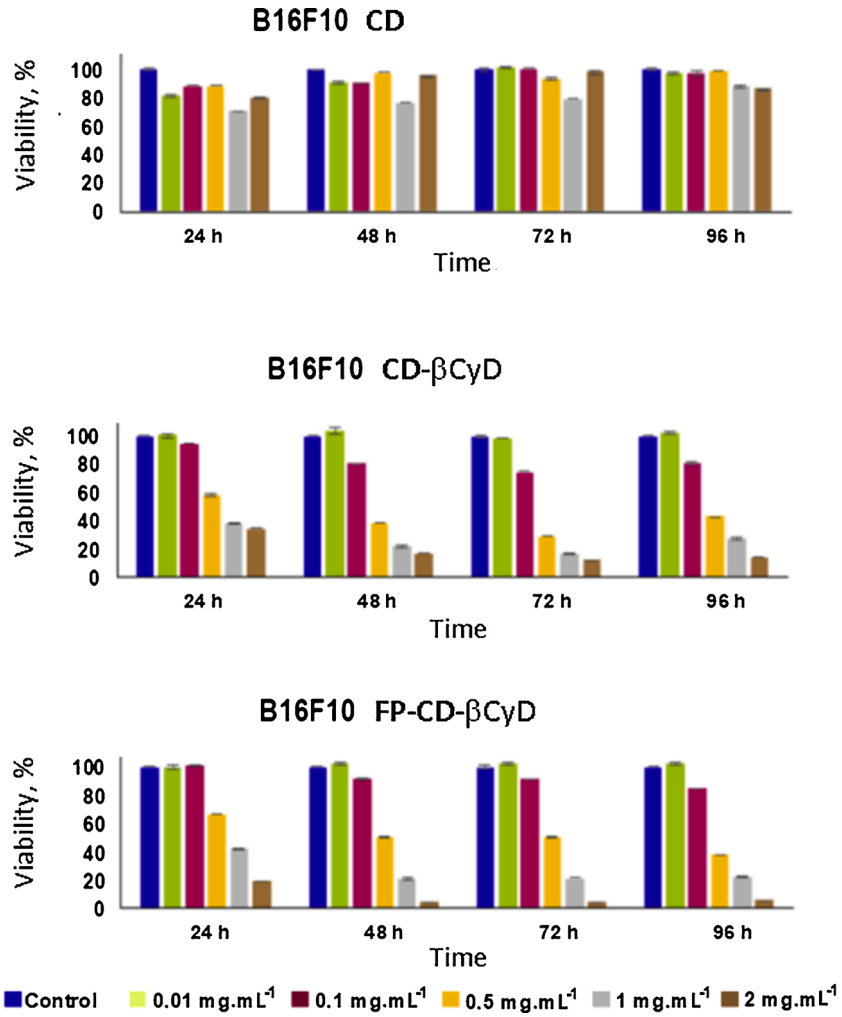

Fig. 7. Cytotoxicity evaluation of B16F10 cells after incubation with different concentrations of CDs, **CD**-βCyDs and **FP-CD**-βCyDs and during different times.

probe itself. In this regard, several reports describe the toxic effects of βCyD to living organisms due to its affinity to cholesterol and to its capacity to solubilize cell membrane lipids [27–29].

Fluorescence microscope images, obtained at 365 nm, 436 nm and 546 nm, showed that **FP-CD**-βCyDs were located at the cytoplasm of treated cells, likely internalized by an endocytosis mechanism [30] (Fig. 8). Furthermore, after cell internalization, a clear contrasted fluorescence signal was observed within each cell with discrete spots indicating specific compartmentalization of the nanoparticles. This images clearly suggest the potentiality of these nanoparticles to be used in cellular bioimaging. These results were confirmed by cell sorting in a cytometer (Fig. S6) in which different cell populations can be distinguished. Thus, the signal of the intensity in the cell population containing **FP-CD**-βCyDs clearly differs from that of the control population and is characterized by higher fluorescence signal within the cells. However, cells containing **CD**-βCyDs cannot be as clearly differentiated from control cells. The fluorescence observed upon excitation at 546 nm may be due not only to the presence of fluorescent proteins in the cells but also to the CDs. In fact, it is well known that the CDs photoluminescence spectrum is excitation-wavelength dependent, undergoing bathochromic shift as the excitation red shifts. Besides, the presence of surface functional groups in CDs such as C═O and CN═ groups can tune the fluorescence of CDs. So, O-related groups (C═O) and N-related groups (C═N) may introduce two new energy levels (HOMO-n_O and HOMO-n_N), thus producing new electron transitions and the red-shift emission occurs when the electrons in C═O or CN═ groups related defect states return to the HOMO [31–34].

Effects of **CD**-βCyDs and **FP-CD**-βCyDs in cell cycle phase distribution of the tumor cell line U2OS in comparison with HMF cells was studied after incubation with 1 mg.mL^{-1} of the corresponding nanoparticles. Fig. 9 shows that HMF cells slightly accumulate in S (DNA synthesis) and G2 (mitosis preparation) phases after incubation with both modified CDs and when compared with control cells. Thus, presence of the fluorescence probes in the CDs may compromise among other things cellular division. On the other hand, cell cycle distribution of U2OS cells was not affected after incubation with **CD**-βCyD or **FP-CD**-βCyD, suggesting the biocompatibility of these nanoparticles with this cell line.

3.3.1. *Intracellular pH*

In cancer cells, cytoplasmic pH may oscillate between 7.2 and 7.5 during cell growth as consequence of cell metabolism, while intracellular pH can oscillate between 6.2 and 6.9 (Warburg effect) [35]. We recently demonstrated [16] that the **FP-CD** fluorescent system was sensitive to pH in aqueous media through a PET (photoinduced electron transfer) process.

In Fig. 10, confocal microscopy images for U2OS cells shows the inactivation of the PET process in the probe at pH 7.4 in comparison with pH 6.0 after incubation with the FP molecule for 30 min. In order to evaluate the potential of **FP-CD**-βCyD as a fluorescent probe for the recognition of cancer cells based on the Warburg effect, we carried out a comparative study with healthy HMF cells and cancerous B16F10 cells treated with 1 mg mL^{-1} CDs, **CD**-βCyD and **FP-CD**-βCyD. The relative intensity data showed that fluorescence after incubation with CD and **CD**-βCyD did not seem to be pH sensitive as marginal differences were

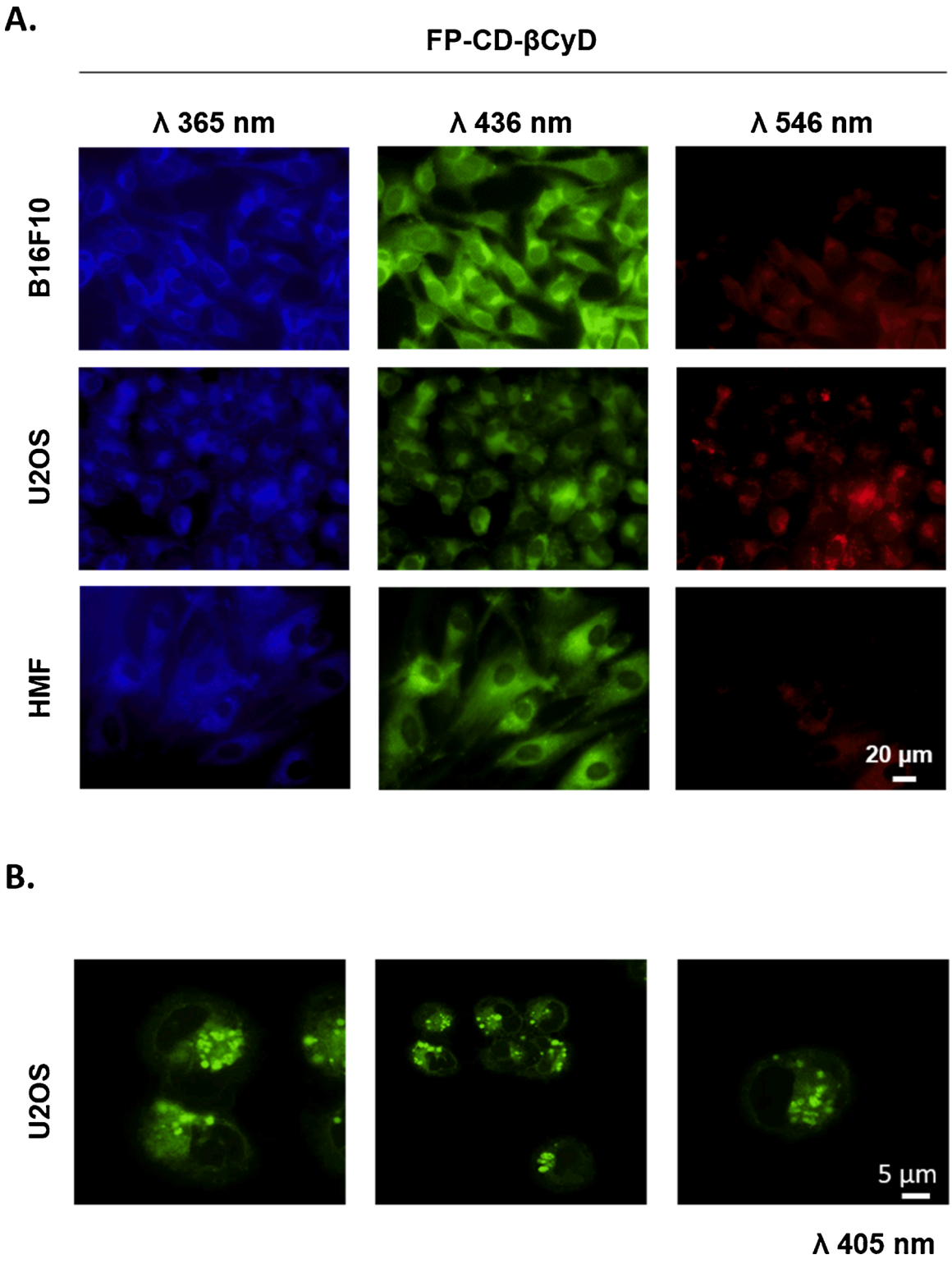

Fig. 8. A. Cell localization of FP-CD-βCyDs after incubation with the indicated cell line. Images were taken at 63x from fixed cells after 1 h incubation at 37 °C with 1 mg mL^{-1} of FP-CD- βCyDs. B. Detailed images of U2OS cells were taken by confocal fluorescence at 63x augmentation showing discrete distribution of FP-CD-βCyDs. Scale is indicated in white.

observed between HMF and B16F10 cells (Fig. 11a). However, there was a significant difference in the fluorescence emission in HMF culture compared to that of B16F10 cells when **FP-CD**-βCyDs were used (2-fold). The mechanism of FP-CD- βCyD interaction with cell surface is suggested in Fig. 11b in which we take into consideration the fact that cyclodextrins are known to interact with components of cell membranes [36]. In this scenario, a possible mechanism that could explain the difference between both cell lines may be based on the interaction of **FP-CD**-βCyDs with the cell membrane. While the βCyD unit of **FP-CD**-βCyDs may penetrate the cell membrane interface forming hydrogen bonds with phosphate and glycerol ester-groups of lipids [37], the **FP** unit can remain exposed towards the external membrane surroundings

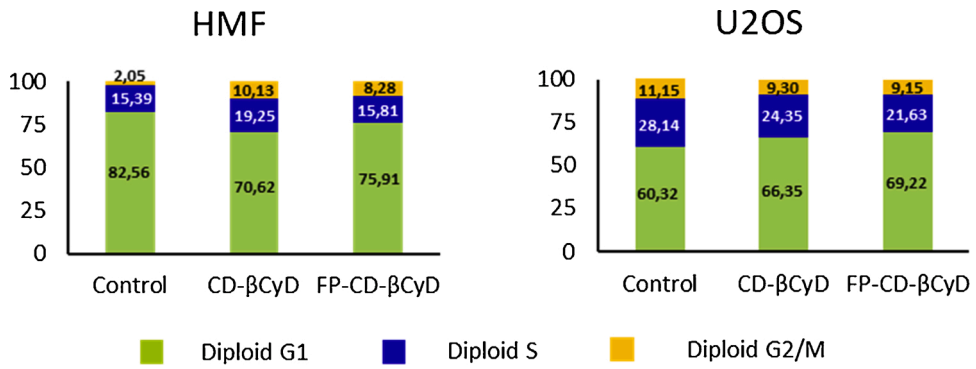

Fig. 9. Cell cycle phase distribution after incubation with 1 mg mL^{-1} of **CD**-βCyD or **FP-CD**-βCyD and in the absence of any CD. Numbers indicate cell percentages at the corresponding cell cycle phase.

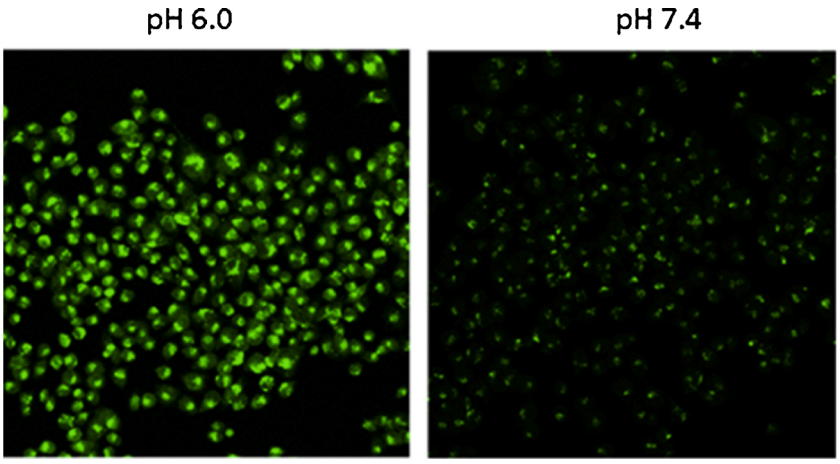

Fig. 10. Fluorescence confocal microscopy images for U2OS cells (63×, laser 405 nm). at pH 6.0 and pH 7.4 in the presence of the **FP** molecule.

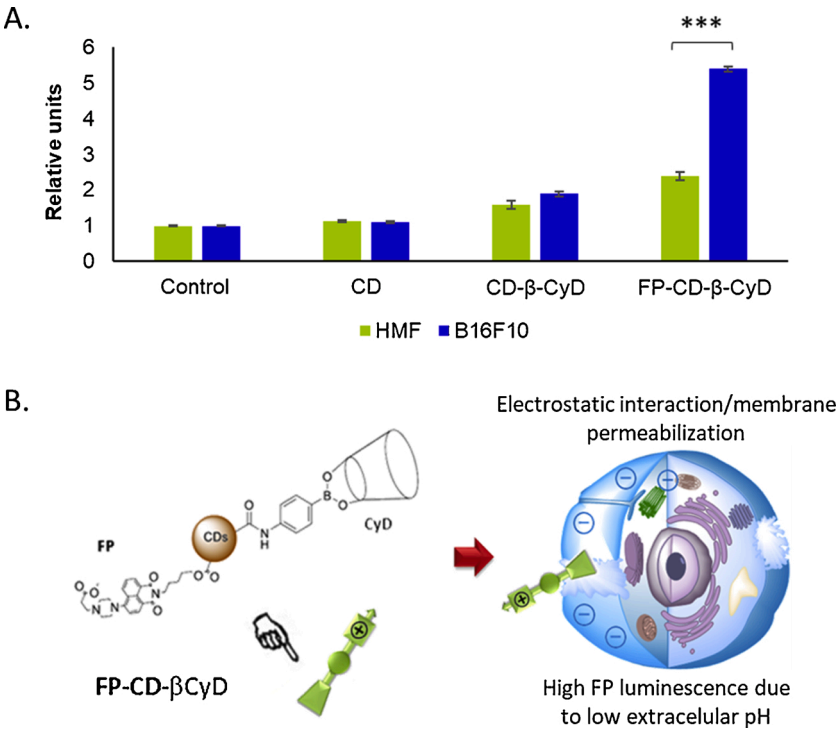

Fig. 11. A. Fluorescence relative intensities of HMF and B16F10 cells after 1 h exposition to 1 mg mL^{-1} of nanomaterials (control: untreated cells). B. Suggested mechanism of **FP** moiety exposure to the cell surface. (*** $p < 0.005$, *t* Student).

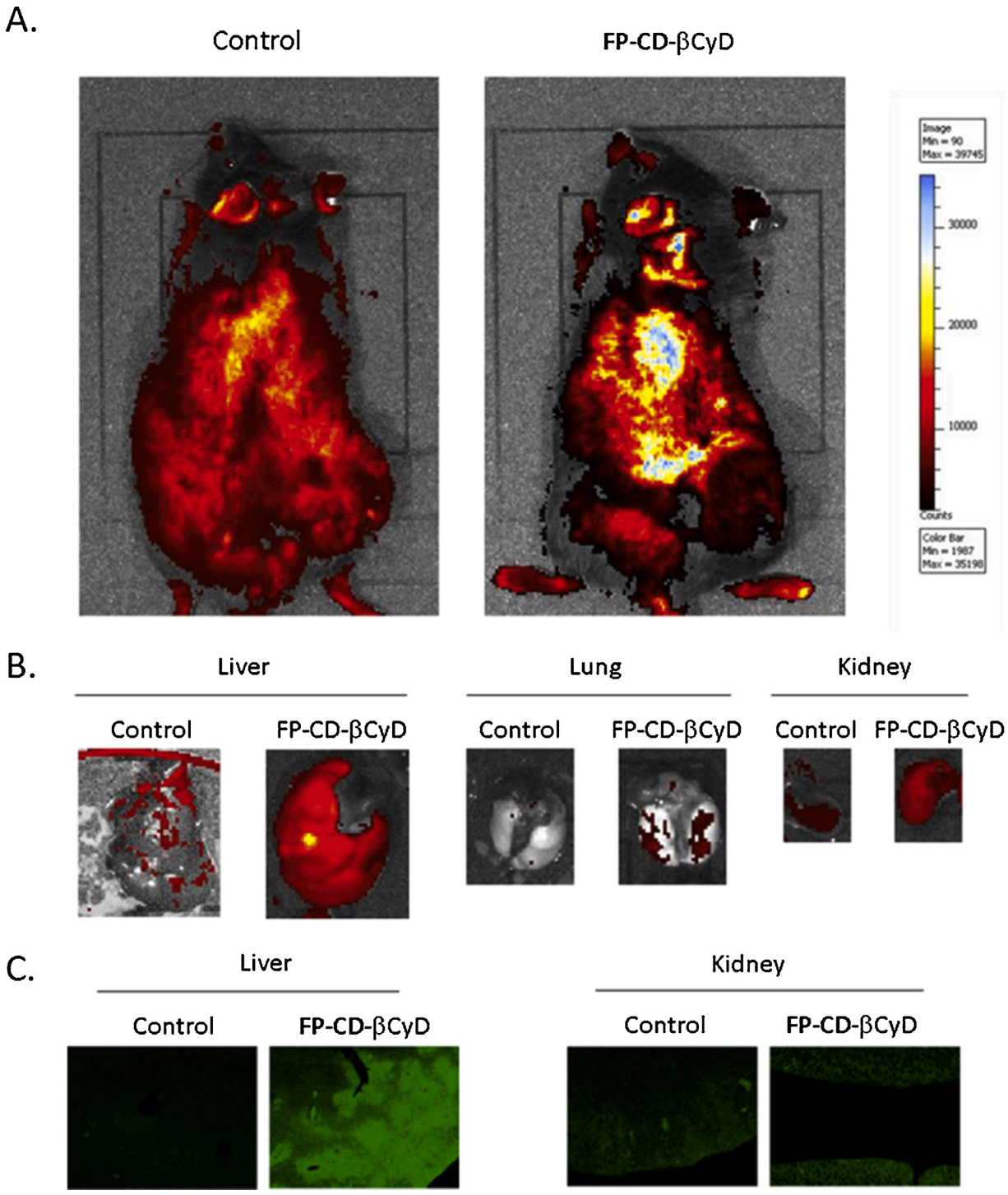

Fig. 12. A. I*n vivo* bioimages of mice 5 min after intravenous injection of **FP-CD**-βCyDs. Left: control mouse with no injection showing autofluorescence. Right: FP-CD-βCyD injected mouse. B. *Ex vivo* images of organs removed 1 h after **FP-CD**-βCyD injection. C. Confocal fluorescence images of liver and kidney tissue slices.

(Fig. 11b). In the case of HMF cells, the **FP** unit was in contact with an intracellular pH 7.2–7.5 and its fluorescence was quenched due to the electron transfer from the nitrogen atoms of the H^+ recognition unit (the piperazine group, pKa = 7.45) to the excited 1,8-naphthylamide signaling subunit (PET process) [16]. On the contrary, when the **FP** unit was in contact with the low pH (6.2-6-4) of B16F10 cells the PET process was blocked and the fluorescence revived when the lone nitrogen atoms of the recognition units were protonated.

3.4. *In vivo studies*

In vivo studies were carried out in mice in order to study the distribution of **FP-CD**-βCyDs in whole organisms after blood injection. Results showed that nanoparticles tend to accumulate in several organs in which higher fluorescence was detected (Fig. 12a). To characterize these organs, mice were sacrificed one hour after **FP-CD**-βCyD injection and then, liver, kidneys and lungs were analyzed. Fluorescence of these organs are shown in Fig. 12b. Results indicated that liver and kidney accumulate more **FP-CD**-βCyDs than lung attending to the level of the

fluorescence intensity. In addition, tissue samples were microtomized and analyzed using confocal fluorescence microscopy, confirming that liver was the organ with the highest amount of **FP-CD**-βCyD (Fig. 12c), probably due to its unique vasculature among the other organs and its role in the transformation of xenobiotics to compounds that the body can eliminate.

4. Conclusions

In this article, glutathione-based carbon nanoparticles have been successfully bi-functionalized. In the first place, with the incorporation of a fluorescent FP label which can be used as a tool to differentiate healthy cells from cells with an acid external pH (typically cancer cells due to Warburg effect). On the other hand, cyclodextrins have also been incorporated as a glucose source, which in turn, eases glycolysis in cancer cells and favors its use as a controlled transport and delivery system for different drugs.

The cytotoxicity studies of these materials in three different cell lines, revealed that, although there is not any visual substantial modification in cell morphology, the βCyD functionalized CDs diminished cell viability and induced alterations in cell cycle phase distribution. In fact, HMF cells seem to be arrested around G2/M phase, something that did not happen with the unfunctionalized CDs.

Likewise, CDs are not only able to get inside the cells and accumulate within discrete points of the cytoplasm, but also to emit fluorescence allowing *in vitro* images with high contrast, especially when using **FP-CD**-βCyDs, whose fluorescence in cancer cell lines is significantly higher than in the noncancerous cell line. In addition, these materials have been used for obtaining *in vivo* fluorescence images after their injection in mice, with an important incidence in those organs with the highest vasculature (mainly liver). These results suggest that these materials are a promising alternative for bioimaging applications.

Finally, from our results we can stand out that the bi-functionalized nanoparticles show a high potential for their use in theranostics as sensor and actuator. Thus, they can be used either as cancer cell marker, because of their ability to identify cells with a slightly acidic environment, as well as to facilitate drug administration during therapy.

Author contribution

Rosana Badía-Laíño and Marta Elena Díaz García conceived and supervised the research; Jorge Espina-Casado and Tania Fontanil developed the experimental work with the same degree of responsibility; Alfonso Fernández-González performed FTIR characterization and data interpretation; Alfonso Fernández-González, R. Badía and Marta Elena Díaz-García wrote the original draft preparation, the revision and edition; S. Cal and A.J Obaya supervised and interpreted the *in vitro* and *in vivo* toxicity experiments; Rosana Badía-Laíño was responsible for funding acquisition and project administration. All authors gave final approval for publication.

Declaration of Competing Interest

The authors declare that they have no known competing financial interests or personal relationships that could have appeared to influence the work reported in this paper.

Acknowledgments

The authors gratefully acknowledge financial support from the Ministerio de Ciencia e Innovación (MCI), Agencia Estatal de Investigación (AEI) and European Regional Development Fund (FEDER), Project # RTI2018-099756-B-I00 (MCI/AEI/FEDER, UE).

Appendix A. Supplementary data

Supplementary material related to this article can be found, in the online version, at doi:https://doi.org/10.1016/j.snb.2021.130555.

References

[1] D. Qu, X. Wang, Y. Bao, Z. Sun, Recent advance of carbon dots in bio-related applications, J. Phys. Mater. 3 (2020), 022003, https://doi.org/10.1088/2515-7639/ab7cb9.
[2] G. Romero, S.E. Moya, Chapter 4 - synthesis of organic nanoparticles, in: J.M. de la Fuente, V. Grazu (Eds.), Frontiers of Nanoscience, Elsevier, 2012, pp. 115–141.
[3] C. Xia, S. Zhu, T. Feng, M. Yang, B. Yang, Evolution and synthesis of carbon dots: from carbon dots to carbonized polymer dots, Adv. Sci. 6 (23) (2019) 4564–4565, https://doi.org/10.1002/advs.201901316.
[4] K. Dimos, Carbon quantum dots: surface passivation and functionalization, Curr. Org. Chem. 20 (2016) 682–695, https://doi.org/10.2174/1385272819666150730220948.
[5] B. Yao, H. Huang, Y. Liu, Z. Kang, Carbon dots: a small conundrum, Trends Chem. 1 (2019) 235–246, https://doi.org/10.1016/j.trechm.2019.02.003.
[6] S. Das, L. Ngashangva, P. Goswami, Carbon dots: an emerging smart material for analytical applications, Micromachines 12 (2021) 84, https://doi.org/10.3390/mi12010084.
[7] L. Liu, L. Chen, J. Liang, L. Liu, H. Han, A novel ratiometric probe based on nitrogen-doped carbon dots and rhodamine isothiocyanate for detection of Fe^{3+} in aqueous solution, J. Anal. Meth. Chem. (2016), 4939582, https://doi.org/10.1155/2016/4939582.
[8] H. Sing, J.S. Sidhu, D.K. Mahajan, N. Singh, A carbon quantum dot and rhodamine-based ratiometric fluorescent complex for the recognition of histidine in aqueous systems, Chem. Front. 3 (2019) 476–483, https://doi.org/10.1039/c8qm00554k.
[9] L.L. Guo, Y.H. Song, K.Y. Cai, L. Wang, 'On-off' ratiometric fluorescent detection of Hg2+ based on N-doped carbon dots rhodamine B@TAPT-DHTA-COF, Spectrochim. Acta Mol. Biomol. Spectrosc. 227 (2020) 1–8, https://doi.org/10.1016/j.saa.2019.117703.
[10] Z. Yu, W. Ma, T. Wu, J. Wen, Y. Zhang, L. Wang, Y. He, H. Chu, M. Hu, Coumarin-modified graphene quantum dots as a sensing platform for multicomponent detection and its applications in fruits and living cells, ACS Omega 5 (2020), https://doi.org/10.1021/acsomega.9b04387, 7369-7368.
[11] Q. Xiao, S. Lu, C. Huang, W. Su, S. Huang, Novel N-doped carbon dots/β-cyclodextrin nanocomposites for enantioselective recognition of tryptophan enantiomers, Sensors 16 (2016) 1874, https://doi.org/10.3390/s16111874.
[12] Z.Y. Lin, Y.C. Kuo, C.J. Chang, Y.S. Lin, T.C. Chiu, C.C. Hu, Highly sensitive sensing of hydroquinone and catechol based on β-cyclodextrin-modified carbon dots, RSC Adv. 8 (2018) 19381–19388, https://doi.org/10.1039/c8ra02813c.
[13] E. de los Reyes-Berbel, I. Ortíz-Gómez, M. Ortega-Muñoz, A. Salinas-Castillo, L. F. Capitan-Vallvey, F. Hernández-Mateo, F.J. López-Jaramillo, F. Santoyo-González, Carbon dots-inspired fluorescent cyclodextrins: competitive supramolecular "off-on" (bio)sensors, Nanoscale 12 (2020) 9178–9185, https://doi.org/10.1039/d0nr01004a.
[14] A.O. Alqarni, S.A. Alkahtani, A.M. Mahmoud, M.M. E-Wekil, Design of "Turn On" fluorimetric nanoprobe based on nitrogen doped graphene quantum dots modified with β-cyclodextrin and vitamin B6 cofactor for selective sensing of dopamine in human serum, Spectrochim. Acta Part A: Mol. Biomol. Spectrosc. 248 (2021), 119180, https://doi.org/10.1016/j.saa.2020.119180.
[15] R.M. Pascale, D.F. Clavisi, M.M. Simile, C.F. Feo, F. Feo, The Warburg effect 97 years after its discovery, Cancers 12 (2020) 2819, https://doi.org/10.3390/cancers12102819.
[16] J. Espina Casado, A. Fernández González, M.E. Díaz García, R. Badía Laíño, Smart carbon dots as chemosensor for control of water contamination in organic media, Sens. Actuators B Chem. 329 (2021), 129262, https://doi.org/10.1016/j.snb.2020.129262.
[17] T. Díaz-Faes López, A. Fernández González, M.E. Díaz-García, R. Badía-Laíño, Highly efficient Förster resonance energy transfer between carbon nanoparticles and europium–tetracycline complex, Carbon 94 (2015) 142–151, https://doi.org/10.1016/j.carbon.2015.06.066.
[18] S. Mondal, P. Purkayastha, A-cyclodextrin functionalized carbon dots: pronounced photoinduced electron transfer by aggregated nanostructures, J. Phys. Chem. C 120 (26) (2016) 14365–14371, https://doi.org/10.1021/acs.jpcc.6b03145.
[19] H. Li, S. Ye, J. Guo, H. Wang, W. Yan, J. Song, J. Qu, Biocompatible carbon dots with low-saturation-intensity and high-photobleaching-resistance for STED nanoscopy imaging of the nucleolus and tunneling nanotubes in living cells, Nano Res. 12 (2019) 3075–3084, https://doi.org/10.1007/s12274-019-2554-x.
[20] N. Liu, M. Tang, Toxicity of different types of quantum dots to mammalian cells in vitro: an update review, J. Hazard. Mater. 399 (2020), 122606, https://doi.org/10.1016/j.jhazmat.2020.122606.
[21] C. Murru, R. Badía Laíño, M.E. Díaz García, Synthesis and characterization of green carbon dots for scavenging radical oxygen species in aqueous and oil samples, Antioxidants 9 (11) (2020) 1147, https://doi.org/10.3390/antiox9111147.
[22] C. Shimpuku, R. Ozawa, A. Sasaki, F. Sato, T. Hashimoto, A. Yamauchi, I. Suzukic, T. Hayashita, Selective glucose recognition by boronic acid azoprobe/γ-cyclodextrin complexes in water, Chem. Commun. (13) (2009) 1709–1711, https://doi.org/10.1039/B819938H.

[23] H. Wang, C. Sun, X. Chen, Y. Zhang, V.L. Colvin, Q. Rice, J. Seo, S. Feng, S. Wang, W.W. Yu, Excitation wavelength independent visible color emission of carbon dots, Nanoscale 9 (5) (2017) 1909–1915, https://doi.org/10.1039/C6NR09200D.
[24] S. Fatimah, S.M. Bilqis, I. Tahir, D. Tahir, Luminescence properties of carbon dots synthesis from sugar for enhancing glows in paints, Mater. Res. Express 6 (9) (2019), 095006, https://doi.org/10.1088/2053-1591/ab2bb7.
[25] D.Y. Guo, C.X. Shan, K.K. Liu, Q. Lou, D.Z. Shen, Surface plasmon effect of carbon nanodots, Nanoscale 7 (2015) 18908, https://doi.org/10.1039/c5nr05918f.
[26] T. Mosmann, Rapid colorimetric assay for cellular growth and survival: application to proliferation and cytotoxicity assays, J. Immunol. Methods 65 (1) (1983) 55–63, https://doi.org/10.1016/0022-1759(83)90303-4.
[27] T. Kiss, F. Fenyvesi, I. Bácskay, J. Váradi, E. Fenyvesi, R. Iványi, L. Szente, A. Tósaki, M. Vecsernyés, Evaluation of the cytotoxicity of β-cyclodextrin derivatives: evidence for the role of cholesterol extraction, Eur. J. Pharm. Sci. 40 (2010) 376–380, https://doi.org/10.1016/j.ejps.2010.04.014.
[28] V.J. Stella, Q. He, Cyclodextrins, Toxicol. Pathol. 36 (2008) 30–42, https://doi.org/10.1177/0192623307310945.
[29] S. Shityakov, R.E. Salmas, E. Salvador, N. Roewer, J. Broscheit, C. Förster, Evaluation of the potential toxicity of unmodified and modified cyclodextrins on murine blood-brain barrier endothelial cells, J. Toxicol. Sci. 41 (2) (2016) 175–184, https://doi.org/10.2131/jts.41.175.
[30] B. Unnikrishnan, R.S. Wu, S.C. Wei, C.C. Huang, H.T. Chang, Fluorescent carbon dots for selective labeling of subcellular organelles, ACS Omega 5 (20) (2020) 11248–11261, https://doi.org/10.1021/acsomega.9b04301.
[31] M. Liu, Optical properties of carbon dots: a review, Nanoarchitectonic 1 (1) (2020) 1–12, https://doi.org/10.37256/nat.112020124.1-12.
[32] K. Jiang, S. Sun, L. Zhang, Y. Lu, A. Wu, C. Cai, H. Lin, Red, green, and blue luminescence by carbon dots: full-color emission tuning and multicolor cellular imaging, Angew. Chem. Int. Ed. 54 (2015) 5360–5363, https://doi.org/10.1002/anie.201501193.
[33] S. Sarkar, M. Sudolská, M. Dubecký, C.J. Reckmeier, A.L. Rogach, R. Zbořil, M. Otyepka, Graphitic nitrogen doping in carbon dots causes red-shifted absorption, J. Phys. Chem. C 120 (2) (2016) 1303–1308, https://doi.org/10.1021/acs.jpcc.5b10186.
[34] K. Holá, M. Sudolská, S. Kalytchuk, D. Nachtigallová, A.L. Rogach, M. Otyepka, R. Zbořil, Graphitic nitrogen triggers red fluorescence in carbon dots, ACS Nano 11 (12) (2017) 12402–12410, https://doi.org/10.1021/acsnano.7b06399.
[35] L. Schwartz, T. Seyfried, K.O. Alfarouk, J.V. Moreira, S. Fais, Out of Warburg effect: an effective cancer treatment targeting the tumor specific metabolism and dysregulated pH, Semin. Cancer Biol. 43 (2017) 134–138, https://doi.org/10.1016/j.semcancer.2017.01.005.
[36] Z. Hammoud, N. Khreich, L. Auezova, S. Fourmentin, A. Elaissari, H. Greige-Gerges, Cyclodextrin-membrane interaction in drug delivery and membrane structure maintenance, Int. J. Pharm. 564 (2019) 59, https://doi.org/10.1016/j.ijpharm.2019.03.063.
[37] W. Khuntawee, P. Wolschann, T. Rungrotmongkol, J. Wong-Ekkabut, S. Hannongbua, Molecular dynamics simulations of the interaction of beta cyclodextrin with a lipid bilayer, J. Chem. Inf. Model. 55 (9) (2015) 1894–1902, https://doi.org/10.1021/acs.jcim.5b00152.

Jorge Espina-Casado received his B.Sc in 2010, his MS in Food Biotechnology in 2012 and his Ph.D. in 2019 from the University of Oviedo with his thesis in the area of nanomaterials. He has been working as Chemical Technician in the Electronic and Vibrational Spectroscopy Unit of the Scientific and Technical Services of the University of Oviedo. He has co-authored several papers and conference contributions related with the basic concepts and applications of fluorescent nanoparticles. His current research interests include applications of luminescent nanoparticles for in-vitro and in-vivo imaging, nanoparticle toxicity studies and fluorescent chemical sensors.

Tania Fontanil received his B.Sc in 2011, her Master's Degree in Biomedicine and Molecular Oncology in 2012 and her Ph.D. in 2017 from the University of Oviedo in the area of Biochemistry and Molecular Oncology. During that time, she participated in both her research and teaching work for the University of Oviedo. She has co-authored several papers and conferences contributions related with the study of modifications in the extracellular matrix in cancer or neurodegenerative diseases progression. She currently works as a research staff at the Ordoñez Institute in the area of advanced therapies (ATMPs).

Alfonso Fernández-González got his B.Sc and Ph.D from the University of Oviedo in 1997 and 2003 respectively. Afterwards, he worked in the Dresden University of Technology (Germany) for two years with Professor Reiner Salzer under the topics of Surface Plasmon Resonance Imaging. From then, he worked in the Spanish Council for Scientific Research and again in the University of Oviedo, where he works as Assistant Lecturer since 2016. He is author of more than sixty scientific papers, reviews and book chapters. His main research interests are the surface analysis in tribology, fluorescence and luminescence, optical sensors and chemometrics.

Álvaro J Obaya received his B.Sc. and his Ph.D. from the University of Oviedo, Spain. He carried out postdoctoral research in different institutions, Newcastle University in UK and Brown University in USA. His research was initially focused in covalent modifications of proteins and afterwards in cell cycle regulation mediated by the protooncogen c-Myc at Prof. John Sedivy's lab at Brown University. He then, was hired at the Instituto Universitario de Oncología del Principado de Asturias (IUOPA, Spain) and performed his research in the characterization of proteases of the ADAMTS family. He is member of the IUOPA and leader of the Tumor Microenvironment group aimed to unravel protein interactions in the extracellular matrix and their functional relevance in tumor development and progression. He is currently Head of the Departmento de Biología Funcional at the Universidad de Oviedo.

Marta Elena Díaz-García received her B.Sc. and PhD. from the University of Oviedo and moved to Loughborough University (U.K.) in 1983 to work with Professor J.N. Miller on Analytical Fluorescence. In 1988 she was promoted to Associate Professor and to Professor in Analytical Chemistry in 1992. Since 2018 is Emeritus Professor at the University of Oviedo, where she continues doing research. As author of more than 170 peer-reviewed articles, reviews and book chapters, her major scientific interests encompass the development and applications of chemical sensors, luminescence techniques, luminescent nanomaterials, micellar media and molecularly imprinted polymers.

Rosana Badía-Laíño received her B.Sc. in chemistry from the National University of La Plata, Argentine, and her Ph.D. from the University of Oviedo, Spain. She carried out postdoctoral research in different institutions in Tijuana (Mexico), Cranfield (United Kingdom) and Madrid (Spain). Her research is mainly focused on development and applications of functional nanomaterials, molecular imprinted sol-gel materials, luminescence spectroscopy and chemical sensors and has published more than 70 papers in reputed SCR journals. She is currently Head of the Department of Physical and Analytical Chemistry at the University of Oviedo.